Tuning the critical current in toroidal superfluids via controllable impurities

Letter

Tuning the critical current in toroidal superfluids via controllable impurities

K. Xhani,[1,2,3] G. Del Pace,[1,2,4,5] N. Grani,[1,2,5] D. Hernández-Rajkov,[1,2,5] B. Donelli,[1,2] G. Roati,[1,2,5] and L. Pezzè[1,2]

[1]*Istituto Nazionale di Ottica del Consiglio Nazionale delle Ricerche (CNR-INO), Largo Enrico Fermi 6, 50125 Firenze, Italy*

[2]*European Laboratory for Nonlinear Spectroscopy (LENS), Via Nello Carrara 1, 50019 Sesto Fiorentino, Italy*

[3]*Department of Applied Science and Technology (DISAT), Politecnico di Torino, 10129 Torino, Italy*

[4]*National Institute for Metrological Research (INRiM), Sesto Fiorentino Office - c/o LENS, Via Nello Carrara, 1 - 50019 Sesto Fiorentino, Italy*

[5]*INFN, Sezione di Firenze, 50019 Sesto Fiorentino, Italy*

(Received 13 November 2025; accepted 20 April 2026; published 21 May 2026)

We combine numerical and experimental approaches to study how impurities affect the maximum superflow in an annular Bose-Einstein condensate. By tuning the impurity density and radial position, we precisely control persistent-current stability: it increases with the number of impurities and when impurities are placed at larger radii. In the unstable regime, the complex vortex motion within the impurity landscape, characterized by pinning and unpinning events, governs the timescale of the current decay and its final value. Our work establishes atomic superfluids as a pristine platform for exploring universal mechanisms of superflow stabilization and decay, paving the way for atomtronic quantum technologies.

DOI: 10.1103/316q-596d

Introduction. Impurities in superfluids and superconductors play a multifaceted role [1,2]. On the one hand, they facilitate vortex nucleation and the associated dissipation, converting nominally lossless flow into resistive dynamics [3,4]. On the other hand, impurities enhance stability by acting as pinning centers that immobilize vortices and suppress energy losses [5]. Vortex pinning is essential for type-II superconductors to sustain dissipationless currents [6,7], while in neutron stars the sudden unpinning of a large number of vortices from the nuclear lattice is thought to trigger the abrupt changes in rotation rate known as pulsar glitches [8,9]. This subtle interplay underlies a broad range of transport phenomena, such as flux flow resistivity, critical currents, phase coherence, and the onset of turbulence [10–12]. Engineering controllable impurities provides a powerful tool to tailor superconducting and superfluid properties, from boosting vortex pinning and critical currents to selecting otherwise unstable phases [13–19]. A key challenge is to identify which impurity attributes (strength, width, magnetic properties, etc.) and spatial correlations control phase stability, transport, and coherence, and to understand how they affect vortex nucleation [20]. Addressing this problem demands advanced numerical simulations to accurately capture the complexity of the disorder present in real materials. An alternative strategy is to engineer platforms where impurities and superfluid dynamics can be precisely controlled and numerical simulations can be performed efficiently.

Ultracold gases provide exactly such a clean platform. Disorder and impurities can be engineered in a controlled manner, for example, via optical speckle potentials [21–23], incommensurate potentials [24], or programmable phase-mask devices [25]. In ring traps, the superflow can be realized in ultraclean conditions, with the multiply connected geometry supporting metastable persistent current states characterized by quantized winding numbers [26–31]. This tunability makes these systems versatile test beds for exploring the interplay of impurities, interactions, and topology in quantum fluids [32–34], with direct atomtronic applications [35–37]. Previous studies have demonstrated that introducing a single impurity in ring superfluids can induce vortex emission, with critical velocities determined by the impurity's characteristics and the ring's size, and with different behaviors for bosonic [38] or fermionic [39,40] superfluids. In contrast, the richer case of multi-impurity systems has remained largely uncharted.

In this work, we follow this bottom-up approach and address the interplay between superflow dissipation and vortex dynamics in the presence of controllable impurities. Our platform consists of a toroidal atomic Bose-Einstein condensate (BEC) whose excitation spectrum is purely collective. We find a stabilization effect analogous to that observed in Josephson-junction necklaces [34], which originates from the multiply connected ring geometry. Here, we trace it to the decrease - with increasing impurity number - of the maximum superfluid velocity normalized to the speed of sound, which inhibits dissipative mechanisms. This result contrasts with recent observations in atomic Fermi superfluids in the Bardeen-Cooper-Schrieffer regime, where Cooper-pair breaking limits the stability of persistent currents [41]. Unlike extended barriers, localized impurities introduce an additional degree of freedom through their radial position. The impurity distribution affects both the maximum superflow velocity and the stability of the persistent current—impurities at larger radii enhance its robustness. The radial position also governs the

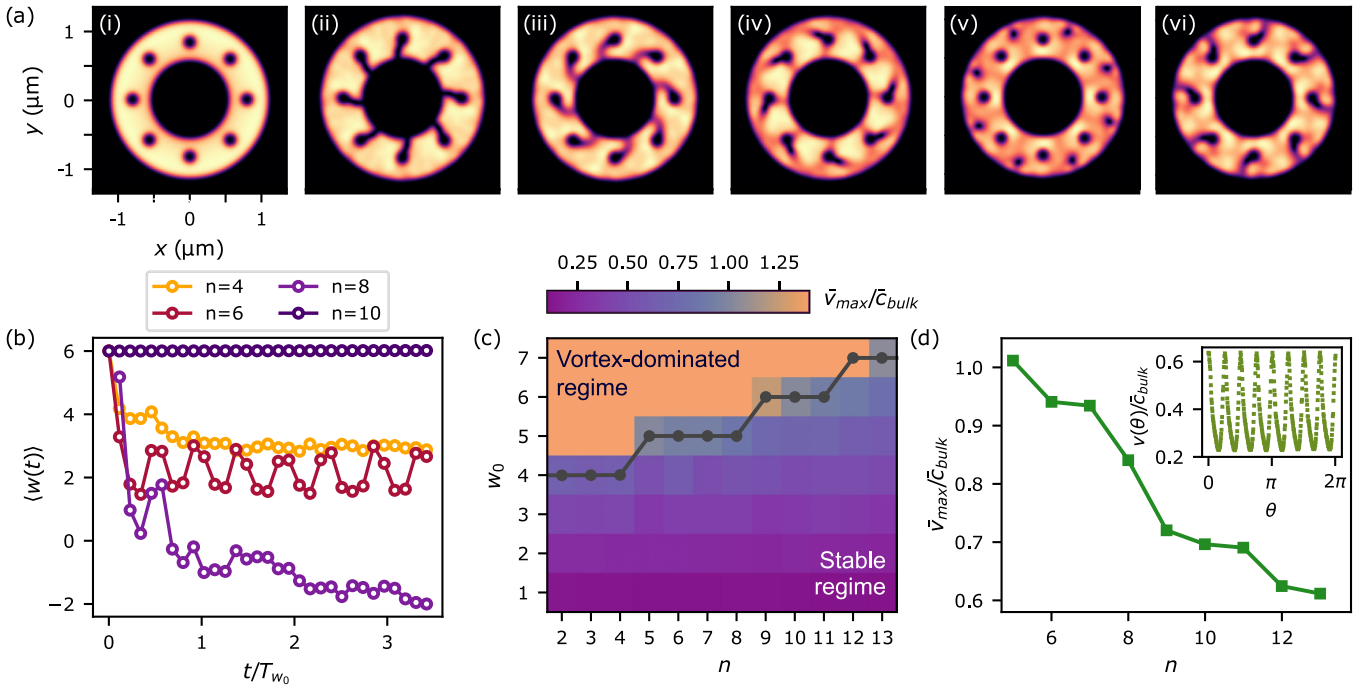

FIG. 1. Phase diagram of a ring superfluid with symmetric impurities. (a) Snapshots of the density in the x-y plane (integrated along the z axis) at different times for the unstable dynamics with $n = 8$ impurities and initial winding $w_0 = 6 > w_c$: $t = 0$ ms (i), 5.7 ms (ii), 7.0 ms (iii), 8.9 ms (iv), 15.3 ms (v), and 20.3 ms (vi). (b) Average winding number $\langle w(t)\rangle$ as a function of time, for different values of n and fixed $w_0 = 6$. The initial temporal evolution (for $t \lesssim 0.5\, T_{w_0}$) for $n = 8$ corresponds to the snapshot shown in panel (a). Times are rescaled in rotation units [47]. (c) Stability phase diagram of the persistent current as a function of n and w_0 in terms of $\bar{v}_{\max}/\bar{c}_{\text{bulk}}$ (see text). The dark gray dots indicate the critical winding number w_c, the solid line is a guide to the eye. (d) Time-averaged superfluid velocity $\bar{v}_{\max}/\bar{c}_{\text{bulk}}$ as a function of n at fixed $w_0 = 5$ and for $n \geqslant 5$, corresponding to the stable configurations for the chosen w_0. The inset reports the angular velocity taken at fixed radius R^* for $w_0 = 5$ and $n = 12$.

vortex emission mechanism: impurities near the center produce symmetric single-vortex emission from each impurity, whereas those near the edge lead to symmetric vortex-dipole emission. Furthermore, vortex-impurity scattering influences vortex dynamics through pinning and unpinning events, which manifest in the time evolution and oscillations of the winding number, as well as in the decay rate and residual current. Experimentally, we recover the two-regime stability diagram, with small deviations due to the imperfect symmetry of the impurity landscape, reducing the current stability in agreement with numerical results.

The system. We study a molecular BEC of ^{6}Li atom pairs confined in a ring potential in the x-y plane, with a tight harmonic confinement along the z axis (see *Appendix A: Numerical methods* for details). The ring has width $\Delta R = R_{\text{out}} - R_{\text{in}} = 11.4$ μm with outer and inner radii of $R_{\text{out}} = 21$ μm and $R_{\text{in}} = 9.6$ μm, respectively. Up to $n \leqslant 16$, repulsive Gaussian obstacles are embedded within the ring, each with a height of $V_0 = 3.7\ \mu$ and a $1/e^2$ width of $\sigma = 1.4$ μm $\simeq 2\xi$. The current is initialized by imprinting a phase onto the condensate wave function. This sets the initial winding number to w_0, such that the initial circulation (at time $t_0 = 0$) is

$$\kappa(R, t_0) = \oint_{\Gamma(R)} v\,(\boldsymbol{r}, t_0)\, d\boldsymbol{r} = \frac{h}{m} w_0, \tag{1}$$

with $\Gamma(R)$ being a circular loop with radius R and centered at the origin, $v(\boldsymbol{r}, t) = (\hbar/m)\nabla\phi(\boldsymbol{r}, t)$ the local superfluid velocity, ϕ the superfluid phase, and m the molecule mass. The condensate dynamics is investigated by solving the three-dimensional time-dependent Gross-Pitaevskii equation (see *Appendix A: Numerical methods*). The supercurrent stability is studied by extracting the temporal evolution of the radially averaged winding: $\langle w(t)\rangle = (m/h)\int_{R_{\text{in}}}^{R_{\text{out}}} \kappa(r, t)dr/\Delta R$. In the absence of impurities, the imprinted winding gives rise to a persistent current, which is stable in time for all the values of w_0 investigated in this work.

Symmetric impurities configuration. We begin by examining the ideal case of identical impurities symmetrically placed at the midradius of the torus, $\bar{r} = (R_{\text{in}} + R_{\text{out}})/2$ [see Fig. 1(a), case (i)]. We find two different dynamical regimes separated by a critical circulation w_c: a stable regime ($w_0 \leqslant w_c$), where the superfluid current remains stable [$w(t) = w_0$], with no vortices emitted into the bulk; and a vortex-dominated regime ($w_0 > w_c$), where the current decays to lower windings with a timescale set by the complex vortex-impurity interaction. An example of supercritical dynamics is shown in Fig. 1(a), cases (ii)–(vi). The onset of vortex emission corresponds to the formation of low-density channels connecting each impurity to the torus's inner boundary [Fig. 1(a), case (ii)], similar to the single-impurity [38,40] or single-barrier [42,43] scenario. Shortly after [Fig. 1(a), case (iii)], n vortices simultaneously enter the condensate through these channels, producing the initial drop in the average winding number [see Fig. 1(b)]. Following their entry, the vortex dynamics become strongly influenced by their interactions with impurities as well as the background superflow [Fig. 1(a), cases (iv)–(vi)]. The strength

of vortex-impurity interactions depends on the impurity parameters, the superflow velocity, and the spatial alignment between vortex cores and impurities [44–46]. For the chosen parameters, vortices tend to spiral partially around impurities before propagating outward toward the torus's outer edge. With weaker impurities, vortices can pass closer to the ring's inner edge without spiraling, indicating a milder vortex-impurity interaction, as occurs for $V_0/\mu < 1$ in the single-obstacle case [38].

The density of impurities further shapes the vortex behavior, especially their pinning events [see Fig. 1(b)]. At low impurity density ($n \leqslant 5$, for the considered parameters), vortices propagate without being pinned, resulting in a decaying winding number. For a higher impurity density (e.g., $n = 6, 7, 8$) at specific initial windings, such as $w_0 = 6$ (i.e., larger initial superflow velocity), vortices experience temporary, weak pinning—brief absorption by impurities—before detaching. These pinning (unpinning) events are reflected by an increase (decrease) of $\langle w \rangle$, which probes not only the superflow dissipation but also the vortex motion, as vortices modify the local superfluid phase profile by causing local phase slippage. Remarkably, for $n = 6$, weak pinning and unpinning events persist over long times and recur periodically, generating nearly sinusoidal oscillations of $\langle w(t) \rangle$ with steady amplitude following the initial decay. The period of oscillations of the current is estimated by T_{w_0}/n, where T_{w_0} is the period of a superflow round trip in the absence of impurities [47]. At a slightly higher impurity density ($n = 8$), pinning dominates the early dynamics, causing $\langle w(t) \rangle$ to dip even below zero—signaling vortex emission beyond the initial winding number $w_0 = 6$, an observation that calls for further investigation of vortex nucleation. After interacting with the impurities, the emitted vortices propagate at the outer edge. Notably, this configuration realizes a current switch: the initial clockwise motion ($w_0 = 6$) relaxes to a counterclockwise circulation [$w(t \gg \tau) = -2$]. Finally, when the impurity density is sufficiently large [e.g., $n = 10$ in Fig. 1(b)], the vortex emission ceases, the winding number remains constant ($w(t) = w_0$), and the supercurrent is preserved over time, marking a stable configuration. The enhanced stability effect for large n, shown in Fig. 1(b), is a general phenomenon that we have observed numerically for different values of superfluid current. The critical winding number w_c separates stable from dissipative flow and increases with n, as shown in the phase diagram of Fig. 1(c). A similar stability enhancement was recently observed in toroidal traps with Josephson-junction arrays [34]. In our setup, impurities are smaller than the ring thickness, with the additional degree of freedom given by the impurity position, rather than the effective one-dimensional case of Josephson barriers [34].

To understand the underlying enhanced-stability mechanism, we examine the local superfluid velocity $v(R^*, t)$, computed at the radius $R^* = \bar{r} - 2\sigma$, between the impurity positions and near the ring's inner boundary, where the velocity peaks and vortices first form [as shown in Fig. 1(a)]. The velocity $v(R^*, t)$ reveals local maxima that oscillate slightly in time due to density fluctuations: we thus compute the time-averaged maximum velocity $\bar{v}_{\max}$ and compare it to the bulk speed of sound $\bar{c}_{\text{bulk}} = \sqrt{g n_{\text{bulk}}/m}$, where $g = 4\pi\hbar^2 a/m$ is the interaction strength and n_{bulk} the bulk density, defined as the maximum density at radius R^*. The color scale in Fig. 1(c) shows the time-averaged ratio $\bar{v}_{\max}/\bar{c}_{\text{bulk}}$ for each pair of n and w_0 values. For $w_0 \leqslant w_c$, the time average covers the full time evolution, while for $w_0 > w_c$ it accounts for only the times before the vortex emission. The critical velocity signaling the onset of dissipation closely matches the time-averaged $\bar{c}_{\text{bulk}}$ and is nearly independent of the impurity number. Specifically, stable configurations satisfy $\bar{v}_{\max}/\bar{c}_{\text{bulk}} < 1$; near the critical point ($w_0 = w_c$) $\bar{v}_{\max}/\bar{c}_{\text{bulk}} \approx 1$; whereas, for $w_0 > w_c$, the ratio $\bar{v}_{\max}/\bar{c}_{\text{bulk}}$ exceeds unity, signaling vortex emission and emergent dissipation. This confirms that dissipation typically begins when the flow velocity surpasses a critical value close to the bulk sound speed, consistent with an interpretation following the Landau criterion. Figure 1(d) also shows that for fixed w_0, e.g., $w_0 = 5$, increasing impurity number n reduces $\bar{v}_{\max}/\bar{c}_{\text{bulk}}$, mainly due to the reduction of $\bar{v}_{\max}$, confirming that higher impurity density enhances stability.

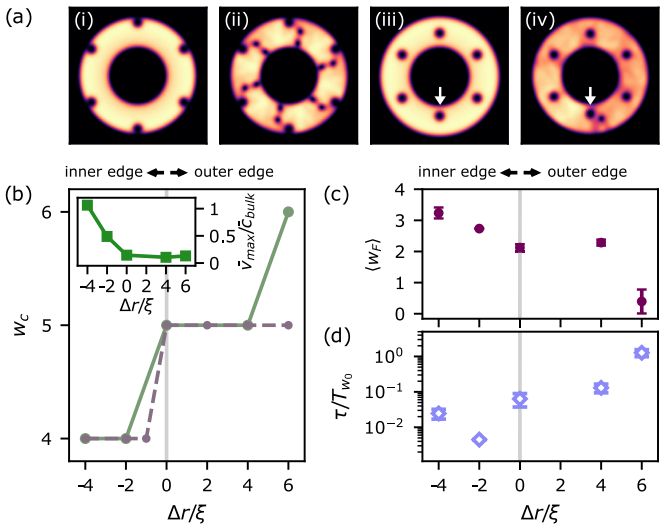

FIG. 2. Role of impurity distribution on the current stability. (a) The two-dimensional condensate density in the x-y plane, initially [cases (i) and (iii)], and after the vortex emission [cases (ii) and (iv)]. Cases (i) and (ii) refer to $n = 6$ impurities displaced at the ring edge, while in cases (iii) and (iv) only one impurity (highlighted by the white arrow) is shifted toward the inner edge, the other impurities being at midradius $\bar{r}$. (b) Critical winding number as a function of the radial position shift $\Delta r/\xi$ for $n = 6$. Green (gray) dots show the case when all (one) impurities are shifted from $\bar{r}$. Lines are guides to the eye. Inset: Scaled superfluid velocity $\bar{v}_{\max}/\bar{c}_{\text{bulk}}$ at fixed $w_0 = 4$ and $n = 6$, in the symmetric configuration where all impurities are displaced by $\Delta r/\xi$. (c) and (d) The final winding number w_F (c) and the decay time τ in rotation units [47] (d) with corresponding error bars as extracted from an exponential fit of the current decay for different impurity shifts $\Delta r/\xi$ in the symmetric configuration. Here we plot the results for the first unstable winding for each impurity configuration, namely, for initial winding $w_0 = w_c + 1$.

Asymmetric impurities configuration. We further investigate how a radial displacement r_0 of the impurities' position from the midradius $\bar{r}$ affects the stability and the vortex emission. Focusing on the case of six impurities, we vary $\Delta r/\xi = (r_0 - \bar{r})/\xi$ from the midradius ($\Delta r = 0$) toward the inner ($\Delta r < 0$) and outer ($\Delta r > 0$) edges. We consider two scenarios [see Fig. 2(a)]: shifting all impurities [cases (i) and

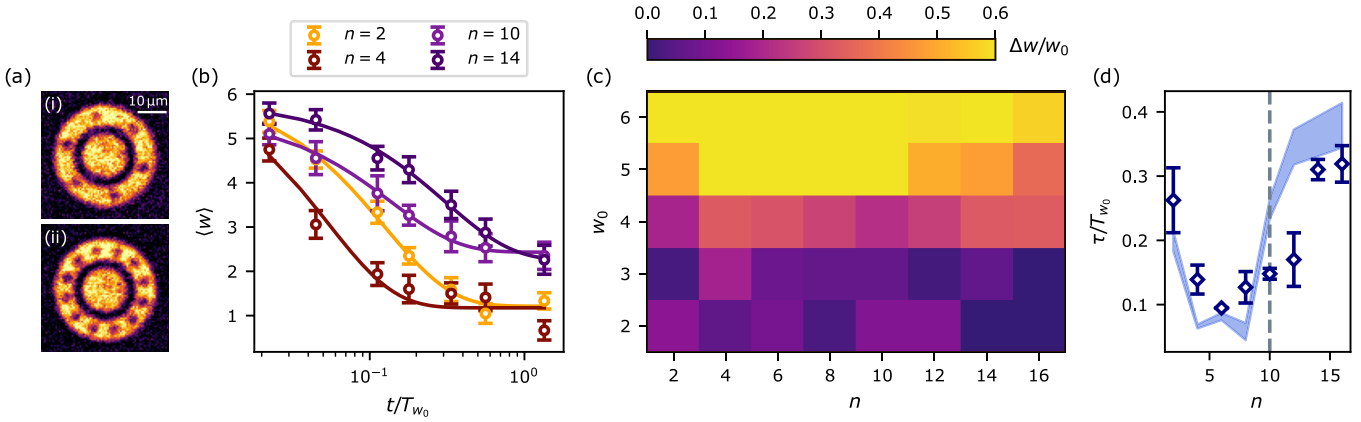

FIG. 3. Experimental results for impurities arranged at the ring center. (a) *In situ* images of the superfluid ring pierced by 6 [case (i)] and 12 [case (ii)] impurities of Gaussian shape with height $V_0/\mu = 3.7(7)$ and width $\sigma = 1.4(1)$ μm (see *Appendix A: Numerical methods*). The central disk provides the phase reference for the interferometric probe of circulation. Each image corresponds to the average over six independent realizations. (b) Measured circulation as a function of time in rotation units [47] for $w_0 = 6$ and different numbers of impurities (see legend). Error bars here represent the standard deviation of the mean value over repeated realizations. The solid lines are exponential fits of the experimental data, from which we extract the decay time τ. (c) Stability diagram for different initial circulations w_0 and number of impurities n. The color scale reports the relative circulation change $\Delta w/w_0 = (w_0 - w_F)/w_0$, where w_F is the average circulation measured at a relatively long time (at least 60 ms). Each data point corresponds to the average over at least two different experimental realizations. (d) Decay time τ extracted from the fit as in panel (b), as a function of the number of impurities for $w_0 = 6$. Circles are experimental results, whereas the blue shaded area shows the results of numerical simulations taking into account fluctuations in the impurities' positions, widths, and heights. The dashed gray line marks the transition value at which the system turns from unstable to stable for identical impurities, i.e., of same heights, widths, and center's positions.

(ii)] or moving just one of them [cases (iii) and (iv)]. Displacing all impurities toward the inner edge lowers the critical winding number w_c, while shifting them outward raises it, as illustrated by the green circles in Fig. 2(b). This trend follows a hydrodynamic reasoning [48]: displacing the impurities outward reduces the maximum local velocity near the impurities [inset of Fig. 2(b)]; therefore, higher w_0 is required to reach the critical flow speed $\sim \bar{c}_{\rm bulk}$. Furthermore, when a single impurity is displaced, the innermost impurity sets the threshold, as shown by the gray dots in Fig. 2(b). In particular, w_c decreases when moving the single impurity toward the center. Instead, when moving the single impurity toward the outer edge of the torus, w_c is determined by the $n-1$ impurities at the midradius and w_c saturates. This configurational dependence also impacts vortex emission and the ensuing dynamics. While symmetric vortex emission is present in periodic impurity arrangements [Fig. 1(a)], displacing a single impurity breaks this symmetry [Fig. 2(a), case (iv)]. Furthermore, for $w_0 > w_c$ when all impurities are moved radially, their position determines the vortex emission type: impurities near the center or inner edge emit single vortices, while those at the outer edge generate vortex dipoles—pairs of a vortex from the inner edge and an antivortex from the outer edge. To quantify this dissipation, the evolution of the averaged winding number is modeled as an exponentially decaying function, $\langle w(t)\rangle = (w_0 - w_F)e^{-t/\tau} + w_F$. Impurities near the inner edge can quickly pin emitted vortices, which stay localized between the impurity and the zero-density center. This strong vortex-impurity interaction stabilizes the current: after a rapid initial drop, $\langle w(t)\rangle$ levels off at a higher final value, w_F [Figs. 2(c) and 2(d)], indicating that only the segment of the ring between the inner edge and the impurity participates in phase slippage. For $\Delta r/\xi = -4$ in Fig. 2(d), vortices shuttle between the impurities and the central region, causing a slightly larger τ than for $\Delta r/\xi = -2$. In contrast, impurities near the outer edge generate vortex dipoles [Fig. 2(a), case (iv)], where antivortices can pin near the impurities during their dynamics, but vortices continue to propagate. This process contributes to a slower decay of $\langle w(t)\rangle$, reaching a lower final circulation w_F [Figs. 2(c) and 2(d)].

Experimental results. Experimentally, we introduce a symmetric configuration of impurities at the midradius of the ring density by shaping a tailored repulsive optical potential using a digital micromirror device (DMD, see *Appendix B: Experimental methods* for details). We monitor their effect on the initial current w_0, which we experimentally verified to be stable in the clean ring, by interfering the ring with a central disk condensate [see Fig. 3(a)] [40]. The experimental results confirm that the system's stability increases with the number of impurities, as illustrated in Fig. 3(b) for $w_0 = 6$. Despite the high resolution of our experimental setup, allowing us to position the impurities with a precision of a fraction of ξ (see *Appendix B: Experimental methods* for details), the experimentally realized impurity configuration deviates from the perfectly symmetric case explored in Fig. 1. This is due to the spatial discretization inherent to the DMD and the limitations on its projection optics, hindering the experimental observation of a fully stable configuration. However, the ratio $\Delta w_F/w_0 = (w_0 - w_F)/w_0$, where w_F is the measured circulation at 180 ms, reveals increasing stability with increasing number of impurities for large w_0, Fig. 3(c), in qualitative agreement with the theoretical analysis of Fig. 1(c). The same behavior is also manifest in the trend of the fitted decay time τ reported in Fig. 3(d)

for $w_0 = 6$, which, after a first drop for small n, increases again for large impurity numbers. This behavior is confirmed by numerical simulations of the current stability in the presence of impurities with properties randomly chosen in the range of the experimental uncertainty (see *Appendix A: Numerical methods*). The numerical simulations also predict an increased stability for large n, without ever recovering a totally stable supercurrent as for the ideal case of an identical, symmetric impurity distribution shown in Fig. 1. Deviations from theoretical behavior may be due to the finite temperature of the experiment, which nevertheless does not preclude the observation of the increased stability.

Conclusions and outlook. This work discussed the stabilization mechanisms induced by multiple impurities in ring superfluids. Future studies should systematically investigate and probe the opposite, unstable, regime, where the interplay of vortex pinning and unpinning could be exploited to program the superflow in the ring. Potential applications include atomtronic dc-to-ac inverters, exploiting the vortex dynamics to induce oscillations of the superfluid current, and atomtronic current reversers that use the simultaneous emission of n vortices to convert clockwise into counterclockwise flow, as shown in Fig. 1(b), see for instance a recent study in one-dimensional systems [49] At present, these engineering possibilities are hindered by the small (submicron) uncertainties in impurity positions, as our analysis shows. Future experimental and theoretical studies could address whether these limitations can be overcome by employing larger impurities or engineered weak links in tailored arrangements, and by accounting for finite-temperature effects, which are expected to modify vortex emission and pinning.

Acknowledgments. We thank Brynmor Haskell for fruitful discussions and Cyprien Daix for contributing to the initial experimental activity at an early stage of this work. K.X. acknowledges funding from the Italian MUR (PRIN DiQut Grant No. 2022523NA7). G.R. and G.D.P. acknowledge financial support from the PNRR MUR project PE0000023-NQSTI. G.R. acknowledges funding from the Italian Ministry of University and Research under the PRIN2017 project CEnTraL and project CNR-FOE-LENS-2024. The authors acknowledge support from the European Union, NextGenerationEU, within the "Integrated Infrastructure Initiative in Photonics and Quantum Sciences" (I-PHOQS). The authors acknowledge funding from INFN through the RELAQS project. This publication has received funding under the Horizon Europe programme HORIZON-CL4-2022-QUANTUM-02-SGA (project PASQuanS2.1, GA No. 101113690) and the Horizon 2020 research and innovation programme (GA No. 871124).

Data availability. The data that support the findings of this article are not publicly available upon publication because it is not technically feasible and/or the cost of preparing, depositing, and hosting the data would be prohibitive within the terms of this research project. The data are available from the authors upon reasonable request.

Appendix A: Numerical methods. We simulate a Bose-Einstein condensate of ^{6}Li molecules, of total mass $M = 2m_{^6\mathrm{Li}}$, in a toroidal trap by solving the three-dimensional Gross-Pitaevskii equation (GPE) [50]. The external potential is $V_{\mathrm{ext}} = V_{\mathrm{harm}} + V_{\mathrm{ring}} + V_{\mathrm{imp}}$, where $V_{\mathrm{harm}} = \frac{M}{2}(\omega_\perp^2 r^2 + \omega_z^2 z^2)$, with $\{\omega_\perp, \omega_z\} = 2\pi \times \{2.5, 396\}$ Hz, and

$$V_{\mathrm{ring}} = V_1\left[\tanh\left(\frac{r - R_{\mathrm{out}}}{\sigma_1}\right) + 1\right] + V_1\left[\tanh\left(\frac{R_{\mathrm{in}} - r}{\sigma_1}\right) + 1\right]. \tag{A1}$$

Here, $R_{\mathrm{in}} = 9.6$ μm, $R_{\mathrm{out}} = 21$ μm, and $\sigma_1 = 0.37$ μm. The barrier height is chosen such that $V_1 > \mu$, so that the density vanishes at the boundaries. For $N = 5100$ molecules, we obtain $\mu = 860$ Hz and healing length $\xi = \hbar/\sqrt{2\mu M} = 0.68$ μm. The impurity potential V_{imp} is modeled as a sum of Gaussian barriers of height V_0 and width σ.

The initial state is obtained by imaginary-time evolution in the presence of n impurities, with an imprinted phase $\exp(-iw_0\theta)$, corresponding to an initial winding number w_0. We then solve the time-dependent GPE and extract the time evolution of the winding number and superfluid velocity. We consider three configurations: (i) symmetric impurities placed at the mean ring radius $\bar{r}$, with $V_0 = 3.7\ \mu$, $\sigma = 1.4$ μm $\simeq 2\xi$; (ii) the same parameters, but with impurity centers displaced from $\bar{r}$; and (iii) a disordered configuration including experimental fluctuations, where impurity height, width, and position are sampled from Gaussian distributions matching the experimental mean values and standard deviations. The results in Fig. 3 are averaged over five realizations for each impurity number n.

Appendix B: Experimental methods. The experiment follows the procedure of Ref. [34,51]. We prepare a molecular ^{6}Li Bose-Einstein condensate in a ring trap with $N \simeq 6 \times 10^3$ atom pairs, a condensed fraction of ∼85%, molecular scattering length $a_M \simeq 1030\, a_0$, and vertical confinement frequency $\nu_z = 396$ Hz. A persistent current with winding number w_0 is generated by phase imprinting, and a repulsive impurity potential is then ramped up in 2.6 ms. In the absence of impurities, the current remains stable over the sample lifetime [38,40] for all the w_0 explored in the study, as we verified by measuring an average winding lifetime as long as the atomic sample lifetime when we introduced no obstacle in the ring. The impurities are created by shaping a 532-nm laser beam with a DMD and imaging it onto the atoms with ∼1-μm resolution. The same setup is also used to produce the ring trap, the central disk, and the azimuthal phase-imprinting gradient. The current is detected interferometrically by overlapping the ring superfluid with the central disk, which acts as a phase reference. In particular, to monitor the current dynamics in the presence of the impurities, we first ramp off the impurity optical potential in 2.6 ms and then proceed with the interferometric detection of the current. We note that the time reported in Fig. 3 is defined as the holding time of the impurity potential at the set value of V_0, thus not accounting for the ramping-up and ramping-down time. Despite being small, the finite duration of the ramping-up time could introduce a shift in the zero of time, as the current could start the decay during the ramping-up process. However, this shift is constant in all datasets at different w_0 and n and does not affect significantly the measurement of the decay time τ, which in fact is found to be in good agreement with numerical simulation results, which do not suffer from this effect.

For a given number of impurities, we measure the mean circulation $\langle w(t)\rangle$ at different holding times, averaging over 15 images, and fit the decay with $w(t) = w_F + (w_0 - w_F)e^{-t/\tau}$, thereby extracting the decay time τ, as shown in Fig. 3(b). The time reported in Fig. 3 denotes the holding time at fixed impurity strength V_0, excluding the ramp times. Any time offset due to the finite ramp-up time is common to all datasets and does not significantly affect τ.

The impurity properties are characterized from CCD images of the DMD light pattern. A two-dimensional Gaussian fit gives the impurity height V_0, width σ, and radial position r_0. Averaging over all configurations with $n \leqslant 16$, we find $V_0/\mu = 3.7(7)$, $\sigma = 1.4(1)$ μm, and $r_0 = 14.9(2)$ μm, with the average aspect ratio of 1.0(1). The numerical simulations in Fig. 3 are obtained by sampling impurity parameters within these experimental confidence intervals. Although the largest relative uncertainty is in the impurity height (20%), it is the submicron positioning uncertainty of <2% that mostly affects the current stability. In fact, the impurities considered in this study have heights well above the superfluid chemical potential: height variations are irrelevant for the supercurrent stability as long as $V_0/\mu > 1$.

[1] P. W. Anderson, Theory of dirty superconductors, J. Phys. Chem. Solids **11**, 26 (1959).

[2] A. A. Abrikosov, On the magnetic properties of superconductors of the second group, Sov. Phys. JETP **5**, 1174 (1957).

[3] M. Tinkham, *Introduction to Superconductivity* (McGraw–Hill, New York, 1996).

[4] G. Blatter, M. V. Feigel'man, V. B. Geshkenbein, A. I. Larkin, and V. M. Vinokur, Vortices in high-temperature superconductors, Rev. Mod. Phys. **66**, 1125 (1994).

[5] A. I. Larkin and Y. N. Ovchinnikov, Pinning in type-II superconductors, J. Low Temp. Phys. **34**, 409 (1979).

[6] A. M. Campbell and J. E. Evetts, Flux vortices and transport currents in type-II superconductors, Adv. Phys. **21**, 199 (1972).

[7] E. H. Brandt, The flux-line lattice in superconductors, Rep. Prog. Phys. **58**, 1465 (1995).

[8] P. W. Anderson and N. Itoh, Pulsar glitches and restlessness as a hard superfluidity phenomenon, Nature (London) **256**, 25 (1975).

[9] B. Haskell and A. Melatos, Models of pulsar glitches, Int. J. Mod. Phys. D **24**, 1530008 (2015).

[10] N. B. Kopnin, Vortex dynamics and mutual friction in superconductors and Fermi superfluids, Rep. Prog. Phys. **65**, 1633 (2002).

[11] W. F. Vinen and J. J. Niemela, Quantum turbulence, J. Low Temp. Phys. **128**, 167 (2002).

[12] C. F. Barenghi, L. Skrbek, and K. R. Sreenivasan, Introduction to quantum turbulence, Proc. Natl. Acad. Sci. USA **111**, 4647 (2014).

[13] B. Maiorov, S. A. Baily, H. Zhou, O. Ugurlu, J. A. Kennison, P. C. Dowden, T. G. Holesinger, S. R. Foltyn, and L. Civale, Synergetic combination of different types of defect to optimize pinning landscape using $BaZrO_3$-doped $YBa_2Cu_3O_7$, Nat. Mater. **8**, 398 (2009).

[14] V. V. Dmitriev, A. A. Senin, A. A. Soldatov, and A. N. Yudin, Polar phase of superfluid ^{3}He in anisotropic aerogel, Phys. Rev. Lett. **115**, 165304 (2015).

[15] R. Wördenweber, Engineering of superconductors and superconducting devices using artificial pinning sites, Phys. Sci. Rev. **2**, 20178000 (2017).

[16] V. Neverov, Correlated disorder as a way towards robust superconductivity, Commun. Phys. **5**, 177 (2022).

[17] M. N. Gastiasoro and B. M. Andersen, Enhancing superconductivity by disorder, Phys. Rev. B **98**, 184510 (2018).

[18] M. Leroux, V. Mishra, J. P. C. Ruff, H. Claus, M. P. Smylie, C. Opagiste, P. Rodière, A. Kayani, G. D. Gu, J. M. Tranquada, W.-K. Kwok, Z. Islam, and U. Welp, Disorder raises the critical temperature of a cuprate superconductor, Proc. Natl. Acad. Sci. USA **116**, 10691 (2019).

[19] M. D. Nguyen, J. Simon, J. W. Scott, A. M. Zimmerman, Y. C. C. Tsai, and W. P. Halperin, Orbital-flop transition of superfluid ^{3}He in anisotropic silica aerogel, Nat. Commun. **15**, 201 (2024).

[20] W.-K. Kwok, U. Welp, A. Glatz, A. E. Koshelev, K. J. Kihlstrom, and G. W. Crabtree, Vortices in high-performance high-temperature superconductors, Rep. Prog. Phys. **79**, 116501 (2016).

[21] J. Billy, V. Josse, Z. Zuo, A. Bernard, B. Hambrecht, P. Lugan, D. Clément, L. Sanchez-Palencia, P. Bouyer, and A. Aspect, Direct observation of Anderson localization of matter waves in a controlled disorder, Nature (London) **453**, 891 (2008).

[22] F. Jendrzejewski, A. Bernard, K. Müller, P. Cheinet, V. Josse, M. Piraud, L. Pezzè, L. Sanchez-Palencia, A. Aspect, and P. Bouyer, Three-dimensional localization of ultracold atoms in an optical disordered potential, Nat. Phys. **8**, 398 (2012).

[23] B. Nagler, M. Will, S. Hiebel, S. Barbosa, J. Koch, M. Fleischhauer, and A. Widera, Ultracold Bose gases in dynamic disorder with tunable correlation time, Phys. Rev. Lett. **128**, 233601 (2022).

[24] G. Roati, C. D'Errico, L. Fallani, M. Fattori, C. Fort, M. Zaccanti, G. Modugno, M. Modugno, and M. Inguscio, Anderson localization of a non-interacting Bose–Einstein condensate, Nature (London) **453**, 895 (2008).

[25] D. H. White, T. A. Haase, D. J. Brown, M. D. Hoogerland, M. S. Najafabadi, J. L. Helm, C. Gies, D. Schumayer, and D. A. W. Hutchinson, Observation of two-dimensional Anderson localisation of ultracold atoms, Nat. Commun. **11**, 4942 (2020).

[26] A. Ramanathan, K. C. Wright, S. R. Muniz, M. Zelan, W. T. Hill, C. J. Lobb, K. Helmerson, W. D. Phillips, and G. K. Campbell, Superflow in a toroidal Bose-Einstein condensate: An atom circuit with a tunable weak link, Phys. Rev. Lett. **106**, 130401 (2011).

[27] S. Moulder, S. Beattie, R. P. Smith, N. Tammuz, and Z. Hadzibabic, Quantized supercurrent decay in an annular Bose-Einstein condensate, Phys. Rev. A **86**, 013629 (2012).

[28] K. C. Wright, R. B. Blakestad, C. J. Lobb, W. D. Phillips, and G. K. Campbell, Driving phase slips in a superfluid atom

circuit with a rotating weak link, Phys. Rev. Lett. **110**, 025302 (2013).
[29] Y. Cai, D. G. Allman, P. Sabharwal, and K. C. Wright, Persistent currents in rings of ultracold fermionic atoms, Phys. Rev. Lett. **128**, 150401 (2022).
[30] J. Polo, W. Chetcuti, T. Haug, A. Minguzzi, K. Wright, and L. Amico, Persistent currents in ultracold gases, Phys. Rep. **1137**, 1 (2025).
[31] A. M. Mateo, A. Gallemí, M. Guilleumas, and R. Mayol, Persistent currents supported by solitary waves in toroidal Bose-Einstein condensates, Phys. Rev. A **91**, 063625 (2015).
[32] S. Eckel, J. G. Lee, F. Jendrzejewski, N. Murray, C. W. Clark, C. J. Lobb, W. D. Phillips, M. Edwards, and G. K. Campbell, Hysteresis in a quantized superfluid atomtronic circuit, Nature (London) **506**, 200 (2014).
[33] S. Eckel, F. Jendrzejewski, A. Kumar, C. L. Lobb, and G. K. Campbell, Interferometric measurement of the current-phase relationship of a superfluid weak link, Phys. Rev. X **4**, 031052 (2014).
[34] L. Pezzè, K. Xhani, C. Daix, N. Grani, B. Donelli, F. Scazza, D. Hernandez-Rajkov, W. J. Kwon, G. Del Pace, and G. Roati, Stabilizing persistent currents in an atomtronic Josephson junction necklace, Nat. Commun. **15**, 4831 (2024).
[35] C. Ryu, E. C. Samson, and M. G. Boshier, Quantum interference of currents in an atomtronic SQUID, Nat. Commun. **11**, 3338 (2020).
[36] L. Amico, D. Anderson, M. Boshier, J.-P. Brantut, L.-C. Kwek, A. Minguzzi, and W. von Klitzing, *Colloquium*: Atomtronic circuits: From many-body physics to quantum technologies, Rev. Mod. Phys. **94**, 041001 (2022).
[37] K. S. Gan, V. P. Singh, L. Amico, and R. Dumke, Josephson dynamics in 2D ring-shaped condensates, arXiv:2509.00533.
[38] K. Xhani, G. Del Pace, F. Scazza, and G. Roati, Decay of persistent currents in annular atomic superfluids, Atoms **11**, 109 (2023).
[39] K. Xhani, A. Barresi, M. Tylutki, G. Wlazłowski, and P. Magierski, Stability of persistent currents in superfluid fermionic rings, Phys. Rev. Res. **7**, 013225 (2025).
[40] G. Del Pace, K. Xhani, A. MuziFalconi, M. Fedrizzi, N. Grani, D. Hernandez Rajkov, M. Inguscio, F. Scazza, W. J. Kwon, and G. Roati, Imprinting persistent currents in tunable fermionic rings, Phys. Rev. X **12**, 041037 (2022).
[41] B. Tüzemen, A. Barresi, G. Wlazłowski, P. Magierski, and K. Xhani, Impurity-controlled vortex mobility and pair-breaking in fermionic superfluid rings, arXiv:2510.24309.
[42] A. I. Yakimenko, K. O. Isaieva, S. I. Vilchinskii, and E. A. Ostrovskaya, Vortex excitation in a stirred toroidal Bose-Einstein condensate, Phys. Rev. A **91**, 023607 (2015).
[43] F. Piazza, L. A. Collins, and A. Smerzi, Vortex-induced phase-slip dissipation in a toroidal Bose-Einstein condensate flowing through a barrier, Phys. Rev. A **80**, 021601(R) (2009).
[44] O. R. Stockdale, M. T. Reeves, and M. J. Davis, Dynamical mechanisms of vortex pinning in superfluid thin films, Phys. Rev. Lett. **127**, 255302 (2021).
[45] I.-K. Liu, S. B. Prasad, A. W. Baggaley, C. F. Barenghi, and T. S. Wood, Vortex depinning in a two-dimensional superfluid, J. Low Temp. Phys. **215**, 376 (2024).
[46] R. Doran, A. J. Groszek, and T. P. Billam, Critical velocity and arrest of a superfluid in a pointlike disordered potential, Phys. Rev. A **109**, 013306 (2024).
[47] We indicate with T_{w_0} the time the superfluid takes to make a loop around the ring at midradius $\bar{r}$ and in the absence of impurities. That is, $T_{w_0} = 2\pi\bar{r}/v(\bar{r}) = 2\pi\bar{r}^2 m/(\hbar w_0)$, where $v(\bar{r}) = \hbar w_0/(m\bar{r})$ is the superfluid speed at $\bar{r}$ for an initial circulation w_0. For the parameters of Figs. 1(a) and 1(b), namely, $w_0 = 6$ and $\bar{r} = 15.3$ μm, we have $T_{w_0} \approx 46$ ms. In Fig. 2(d), for each point we account for the corresponding set by the initial winding w_0.
[48] R. Dubessy, T. Liennard, P. Pedri, and H. Perrin, Critical rotation of an annular superfluid Bose-Einstein condensate, Phys. Rev. A **86**, 011602(R) (2012).
[49] G. Nesti and L. Pezzè, Increasing the stability of a superfluid in a rotating necklace potential, arXiv:2601.15159
[50] The GPE is solved numerically by the Fourier split-step method on a Cartesian grid of $\{N_x, N_y, N_z\} = \{256, 256, 80\}$ points dividing a grid size of length $-34.846\ \mu\text{m} \leqslant r \leqslant 34.846\ \mu\text{m}$ and $-11.0\ \mu\text{m} \leqslant z \leqslant 11.0\ \mu\text{m}$ in the radial plane and axial direction, respectively. The time step is instead set to $\Delta t = 1 \times 10^{-5}\omega_\perp^{-1}$.
[51] A. Kumar, R. Dubessy, T. Badr, C. De Rossi, M. de Goër de Hervé, L. Longchambon, and H. Perrin, Producing superfluid circulation states using phase imprinting, Phys. Rev. A **97**, 043615 (2018).